Received: 17 March 2023 | Revised: 11 September 2023 | Accepted: 1 October 2023

DOI: 10.1002/qj.4591

Quarterly Journal of the Royal Meteorological Society
RMetS

RESEARCH ARTICLE

Neutral and stratified turbulent boundary-layer flow over low mountains

Francois Lott[1] | **Anton Beljaars**[2] | **Lucile Pauget**[1,3] | **Bruno Deremble**[4]

[1]Universite PSL, Ecole Normale Supérieure, Département des géosciences, Laboratoire de Météorologie Dynamique, Paris, France

[2]Research Department, European Centre for Medium-Range Weather Forecasts, Reading, UK

[3]Département Analyse Surveillance Environnement, Commissariat à l'Energie atomique/DAM, Bruyères le Chatel, France

[4]Institut des Géosciences de l'Environnement, University Grenoble Alpes, Grenoble, France

Correspondence
Francois Lott, Laboratoire de Météorologie Dynamique, Ecole Normale Supérieure, 24 rue Lhomond, 75231 Paris, France.
Email: flott@lmd.ens.fr

Funding information
Laboratoire Conventionné Yves Rocard BLOWAVES; VESRI-Schmidt Future: Datawave project

Abstract

A theory for flow over gentle hills using a mixing-length turbulence closure is developed to describe the transition from turbulent orographic form drag to gravity wave drag. It confirms that the first is associated with downstream sheltering, and the second with upstream blocking and strong downslope winds. It shows that the altitude at which the incident flow needs to be taken to calculate the drag is the inner layer scale at which dissipation equilibrates disturbance advection. It also shows that the parameter that controls the transition, here a Richardson number, compares the mountain length with the altitude of the turning points above which the upward-propagating gravity waves become evanescent. Our solutions are also used to show that the downslope winds penetrate well into the inner layer and that a good fraction of the drag is deposited in the inner layer: all of it in the neutral case, a large fraction in the intermediate cases when there are trapped lee waves, and even in stable situations without trapping part of the gravity wave drag is eroded in the inner layer. Some discussion on how to combine neutral and stratified effects in the parametrization of subgrid scale orography in large-scale models is given.

KEYWORDS

flow blocking, mountain drag, mountain waves, neutral and stratified boundary layers, Reynolds stress, sheltering effect

1 | INTRODUCTION

Topographies with small horizontal scale L are assumed to produce disturbances with amplitude exponentially decaying in the free atmosphere (evanescent waves), hence essentially affecting the boundary layer. The modification of turbulent dissipation (and induced stress) results in mountain drag forces that can substantially increase the turbulent drag (Hunt et al., 1988a). In this case, the drag is related to downstream "non-separated" sheltering with the pressure loss across the hill being caused by frictional retardation of the flow near the surface when the slopes are sufficiently small or by flow separation on the downstream side when the slopes are large—see, for instance, the large-eddy simulations in Allen and Brown (2002) and Reinert et al. (2007). A pretty illustration of such downstream separation and the associated circulations is the formation of banner clouds, which sometimes appear in the right conditions (Voigt & Wirth, 2013). For mountains with bigger horizontal length scale and in the presence of stratification, buoyancy force can act against downstream sheltering, forcing an intense flow along the downstream flank of the hill. The mechanism at work in this case is related to buoyancy/gravity waves and is efficient for two reasons. The first reason is that in the presence of internal waves the disturbance amplitudes no longer decay exponentially with altitude in the free atmosphere, which means that the dynamics is no longer limited to the boundary layer. The second reason is that, close to the surface, the horizontal and vertical winds have opposite phase; that is, large horizontal wind occurs when the vertical velocity is negative, which is the fundamental mechanism causing downslope winds—see more details in the review by Durran (1990). Still in these conditions, the wind also becomes weak upstream, causing upstream blocking for large mountains—some recent observations and large-eddy simulations are found in Pokharel et al. (2017) and Sauer et al. (2016). In these stratified cases, the drag is caused by mountain waves for low hills and blocked flow drag for mountains of sufficient height.

Although these contrasting dynamics can be studied in great detail using high-resolution models (Finnigan et al., 2020), the transition between the two regimes has not received much attention. To our knowledge, only a few articles address this transition explicitly. Belcher and Wood (1996) analyse theoretically the transition from form drag to wave drag, the form drag being related to non-separated sheltering gradually being replaced by wave drag when stratification increases. The transition has also been analysed in wind-tunnel experiments and numerical simulations by Ross et al. (2004) or in the prediction of where flow separation is likely to occur (Ambaum & Marshall, 2005). The fact that the transition itself is not much studied does not mean that the interplay between boundary layers and mountain waves has never been analysed. Numerous articles analyse the impact of the boundary layer on mountain waves (Richard et al., 1989; Smith et al., 2006) or on the trapped waves developing at a boundary-layer inversion (Sachsperger et al., 2015; Teixeira et al., 2013a). The fact that some wave drag in the boundary layer can be significant was also recognized by Tsiringakis et al. (2017) and earlier by Chimonas and Nappo (1989). Beyond the drag itself, the contribution of boundary-layer waves to turbulent exchange is also recognized in oceanography and for sediment suspension (Boegman & Stastna, 2019; Soontiens et al., 2015).

The purpose of this study is to revisit early theories about the interactions between mountain and boundary layer in the neutral and stratified case. For this purpose we return to theories dating back from the 1980–1990s (Belcher & Wood, 1996; Hunt et al., 1988a; Hunt et al., 1988b) and complement them by deriving uniform approximations that capture smoothly the transitions between the so-called "inner" and "outer" regions. As we will see, the solutions we obtain capture all together the rich quasi-"inviscid" dynamics associated with the conventional mountain wave theory (which includes trapped lee waves) and its explicit interaction with the boundary-layer dynamics (for instance, the extent to which downslope winds penetrate into the inner layer). Our study also has a more practical motivation: there are two families of subgrid-scale orography parametrizations in present-day weather forecast and climate models. A first family represents the enhancement of turbulent drag by orography (Wood & Mason, 1993), with parametrizations that are today improved to represent better nonlinear effects and the vertical distribution of the drag (Beljaars et al., 2004; Wood et al., 2001). A second family represents a dynamics controlled by gravity waves (Palmer et al., 1986) and that has also been extended to include nonlinear effects (Lott & Miller, 1997). It is generally assumed that the first type of parametrization, also called "turbulent orographic form drag", should act for mountains of scale $L < 5\,\mathrm{km}$ typically, whereas the second type, also called "subgrid-scale orography" (SSO) should consider large-scale mountains (Beljaars et al., 2004). With increasing model resolution it could be argued that only the turbulent orographic form drag parametrizations should stay in the future, the gravity wave part being explicitly resolved, but we are probably still far from this status. A first reason is that the effective resolution of weather forecast models can be near an order of magnitude coarser than the model grid size (Vosper et al., 2016). A second reason is that the $L = 5\,\mathrm{km}$ cut-off is quite arbitrary and should be determined according to the local condition before removing the SSO-type schemes. A third reason is that even if a model can potentially resolve the small-scale gravity waves, they will certainly interact with some form of turbulent parametrization; understanding theoretically the interaction remains important.

In a recent series of papers, Lott and co-workers (Lott et al., 2020a; Lott et al., 2020b; Soufflet et al., 2022) formulated such theory and presented uniform solutions in the constant eddy-viscosity case for small slopes S. They show that the disturbance amplitude is near that predicted using inviscid theory if one takes for incident wind its value at altitude near the inner layer scale δ where dissipative effects equilibrate disturbance advection:

$$\frac{U_0(\delta)}{L} \approx \frac{\nu'(\delta)}{\delta^2}, \tag{1}$$

U_0 and ν' respectively being the incident wind and the eddy diffusivity acting on the disturbance. Lott et al. (2020b) then describe the transition from neutral to stratified and show that the transition occurs when the Richardson number $J \approx 1$ (see Section 2.1). To interpret this result they estimated in their eq. (33) the turning point altitude where the Scorer parameter satisfies

$$S_c(h_t) = \frac{N(h_t)^2}{U(h_t)^2} - \frac{U_{zz}(h_t)}{U(h_t)} = 1/L^2, \tag{2}$$

where h_t is the altitude above which the disturbance with wave number $1/L$ becomes evanescent in the vertical direction. In Lott et al. (2020b), the turning level was found to be approximately at $h_t \approx \sqrt{J}\,L$. With $J < 1$ ($J > 1$) the turning level is close to (far from) the surface compared with the mountain length, and we argued that the gravity waves have not (have) enough vertical space to develop and the dynamics is neutral (stratified). When the wind is sheared in the boundary layer and becomes constant above, Soufflet et al. (2022) found that the Richardson number in the boundary layer, but above the inner layer, is still the appropriate parameter to estimate the nature of the dynamics. In all cases we found that the transition from neutral to stratified is also a transition from downstream sheltering to upstream blocking when the height of the mountain approaches the inner layer scale (Lott et al., 2020b; Soufflet et al., 2022). Soufflet et al. (2022) also revealed the significance of the trapped lee waves during the transition (when $J \approx 1$) and the redistribution of the pressure drag in terms of vertical and horizontal pseudo momentum flux.

Since the constant-viscosity model is too simple to represent the real eddy diffusivity, particularly its decay when approaching the surface, the purpose of this article is to extend the formalism in Lott et al. (2020a), Lott et al. (2020b), and Soufflet et al. (2022) by using a first-order mixing-length closure reminiscent of the one used in Belcher and Wood (1996).

The plan of the article is as follows. In Section 2 we recall the basic equations and give an outline of the theory used in comparison with the theories used in the past. In Section 3 we describe the transition from downstream sheltering to upstream blocking and describe the trapped waves that develop strongly during the transition. In Section 4 we present diagnostics of mountain drag and Reynolds stresses profiles. In Section 5 we summarize and discuss the significance of our results in the context of subgrid-scale orography parametrization. We also relate them to the results in Belcher and Wood (1996). The model is detailed in the Appendix; it combines asymptotic developments and numerical integrations of the inner layer equations using a curved coordinate formalism.

2 | BASIC EQUATIONS

2.1 | Boussinesq equations and mixing length

All our calculations use the Boussinesq approximation written in hybrid terrain following coordinates (X, Z), which are related to the Cartesian coordinates (x, z) via

$$x = X, \quad z = Z + h(X)f(Z) = Z + z', \tag{3}$$

where $h(x)$ is the mountain height and the function $f(Z)$ is positive. $f(Z)$ ensures the transition from terrain-following coordinates near the surface to Cartesian coordinates by taking $f(0) = 1$ and decaying towards zero for $Z \rightarrow \infty$. From Clark (1977), it can be shown that the stationary Boussinesq equations can be written as follows:

$$\rho(u\partial_X u + \mathrm{W}\partial_Z u) = -(\partial_X \rho p + \partial_Z \rho g_{12} p) + \partial_Z \tau_{XZ}, \tag{4a}$$

$$\rho(u\partial_X w + \mathrm{W}\partial_Z w) = -\partial_Z p + \rho b + \partial_Z \tau_{XZ}, \tag{4b}$$

$$\rho(u\partial_X b + \mathrm{W}\partial_Z b) = \partial_Z q_Z, \tag{4c}$$

$$\partial_X \rho u + \partial_Z \rho \mathrm{W} = 0, \tag{4d}$$

where the "pseudo" density ρ is the Jacobian of the coordinate transformation, ρg_{12} is a metric tensor coefficient, and W a velocity in the direction perpendicular to the Z =constant surfaces:

$$\rho = \partial_Z z, \quad \rho g_{12} = -\partial_X z, \quad \mathrm{W} = u\partial_x Z + w\partial_z Z, \tag{5}$$

where u and w are the horizontal and vertical velocities. Compared with Clark (1977), we have rather followed the common practice to neglect the stresses and heat flux in the horizontal direction (τ_{XX}, τ_{ZX}, and q_X), which is consistent with the mixing-length model we will adopt. Finally, in Equations 4a–4d we have divided pressure anomaly by a constant reference density ρ_s—$(p - p_s(z))/\rho_R \rightarrow p$—and the buoyancy $b = -g(\theta - \theta_s)/\theta_s$, where θ is potential temperature and θ_s a reference value.

In general, we will assume no slip and no flow boundary conditions at the surface:

$$u(Z = 0) = \mathrm{W}(Z = 0) = b(Z = 0) = 0. \tag{6}$$

To express the stress tensors, we use a closure for eddy diffusivity based on mixing length theory:

$$\tau_{XZ} = \nu\partial_Z u, \quad \tau_{ZZ} = \nu\partial_Z w, \quad q_Z = \nu\partial_Z b, \quad \text{with } \nu = \Lambda_0^2\left\|\frac{\partial u}{\partial Z}\right\|, \tag{7}$$

where Λ_0 is the mixing length. Standard atmospheric boundary-layer models for neutral flow often have a smooth transition from the linear increase of mixing length near the surface to a constant limit value λ far away from the surface; for instance, according to the so-called

Blackadar formulation:

$$\frac{1}{\Lambda_0} = \frac{1}{\kappa(Z+z_0)} + \frac{1}{\lambda}, \tag{8}$$

where κ is the von Karman constant and z_0 a roughness length. As λ limits the mixing above the surface layer it could vary with stratification, a constraint we did not include explicitly. Note, nevertheless, that our calculations will cover a large range of λ, with more stable cases being related to smaller values of this parameter. A difficulty with the mixing-length profile in Equation (8) is that the background flows that give uniform fluxes have a logarithmic contribution that extends up to $z = \infty$—see Belcher and Wood (1996). As log-layers are confined to the near surface and to simplify the theory, we slightly modify the formula for the mixing length in Equation (8) and take

$$\Lambda_0 = \lambda \tanh\left(\kappa \frac{Z+z_0}{\lambda}\right). \tag{9}$$

This approximation keeps $\Lambda \approx \kappa Z$ near the surface and $\Lambda \approx \lambda$ in the far field. With this expression, the horizontal wind and buoyancy profiles that give uniform fluxes are

$$\begin{aligned} U_V(Z) &= \frac{u_*}{\kappa} \log\left[\frac{\sinh \kappa(Z+z_0)/\lambda}{\sinh \kappa z_0/\lambda}\right], \\ B_V(Z) &= \frac{b_*}{\kappa} \log\left[\frac{\sinh \kappa(Z+z_0)/\lambda}{\sinh \kappa z_0/\lambda}\right], \end{aligned} \tag{10}$$

where the subscript V denotes the background "viscous" solutions, $u_* = \sqrt{\tau_s/\rho_R}$ is the friction velocity, and $b_* = gH_s/(\rho_s c_p u_* \theta_s)$ is the buoyancy scale, with τ_s and H_s for surface stress and heat flux and c_p for the air heat capacity per unit mass at constant pressure.

Another difficulty when one tries to analyse the interaction between mountain waves and a dissipative surface layer is that the velocity in Equation (10) keeps increasing with altitude, which is not realistic. The vertical profiles also tend to confine vertically propagating gravity waves to low altitudes. This can spuriously limit the contribution of the gravity waves to the Reynolds stress for instance. To circumvent this issue, we will consider cases where the wind profile is modified to become constant above a height d:

$$\begin{aligned} U_0(Z) &= \frac{u_* d}{\lambda} \tanh\left[\frac{\lambda}{u_* d} U_V(Z)\right], \\ B_0(Z) &= B_V(z). \end{aligned} \tag{11}$$

This introduces a boundary-layer depth d above which the background flow is externally imposed rather than being an exact solution of the viscous equations. Note that the case with infinite winds in the far field, Equation (10), can be obtained with Equation (11) by taking $d = \infty$.

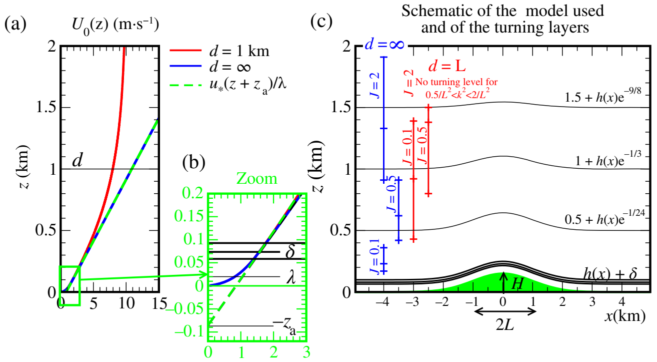

FIGURE 1 (a, b) Background winds used and their various fits according to layer properties (see legend) $\lambda = 20\,\text{m}$, $z_0 = 1\,\text{m}$, $L = 1\,\text{km}$, $d = 1\,\text{km}$, $u_* = 0.2\,\text{m}\cdot\text{s}^{-1}$. (c) Schematic of the model used. The three thin black solid lines follow the surfaces $Z = 0.5, 1, 1.5$. In (b) and (c) the thick black almost horizontal lines span the inner layer scales corresponding to the dominant harmonics excited by a Gaussian mountain ridge of horizontal scale L. In (c) the vertical lines indicate the location and depth of the turning layer spanned by the turning levels according to Equation (2): cases with $d = \infty$ ($d = L$) are in blue (red). The central crosses are for the dominant wave number $k = 1/L$.

As an illustrative example, Figure 1 shows the background wind profiles for $d = 1\,\text{km}$ and $d = \infty$ in a configuration that is characteristic for the cases we will analyse. For mountainous areas, typical values for roughness length, the limit value of the mixing length, friction velocity, boundary-layer depth, and the mountain length scale are

$$\begin{aligned} &z_0 = 1\text{ m}, \lambda = 20\text{ m}, u_* = 0.2\text{ m}\cdot\text{s}^{-1}, \\ &d = 1\text{ km}, L = 1\text{ km}. \end{aligned} \tag{12}$$

The choice for z_0 corresponds to that often made over chaotic surfaces (Wieringa, 1992), whereas that for λ is consistent with observations (Sun, 2011). In Figure 1a one sees that when $d = \infty$, U_0 has constant shear over almost the entire domain, whereas when $d = 1\,\text{km}$, the constant shear zone is limited to the boundary layer where $z < d$. Henceforth, we will call cases using $d = \infty$ "constant-shear" cases and cases using $d \neq \infty$ "variable-shear" cases. Note that to analyse cases where all harmonics propagate aloft, we will also consider hydrostatic solutions when $d \neq \infty$.

The zoom near the surface in Figure 1b shows that, when approaching the surface, the background wind transitions from a linear profile to a log-profile around $z = \lambda$. We will call the logarithmic domain of the profile the surface layer. Figure 1a,b also shows the linear asymptote of U_0 when $\lambda \ll z \ll d$, illustrating that

$$U_0(z) \underbrace{\approx}_{\lambda\ll z\ll d} \frac{u_*(z+z_a)}{\lambda}, \quad B_0(z) \underbrace{\approx}_{\lambda\ll z} \frac{b_*(z+z_a)}{\lambda}, \tag{13}$$

where the parameter

$$z_a = z_0 - \frac{\lambda}{\kappa}\log\left(2\sinh\frac{\kappa z_0}{\lambda}\right) \tag{14}$$

measures the depth of the "critical level": at $z = -z_a$ all disturbances have null intrinsic phase speed. At least in the boundary layer and above the surface layer, these asymptotes match U_0 and B_0 quite well. An important measure of the flow stability is the background flow Richardson number:

$$Ri(z) = \frac{B_{0z}}{U_{0z}^2}. \tag{15}$$

From the flow profiles in Equation (11), it is clear that $Ri(z)$ is zero near the surface, constant and equal to parameter J in the shear zone, and infinite when $z \gg d$. Parameter J is defined as

$$J = Ri(\lambda \ll z \ll d) = \lambda\frac{b_* u_*}{u_*^3} = \frac{\lambda}{\kappa L_{mo}}, \tag{16}$$

where L_{mo} is the Obukhov length. Though in principle the characteristic length λ should be related to L_{mo}, we have chosen to keep them separated in order to disentangle the dynamical impact of J through the inviscid dynamics and of the turbulence (and hence λ or z_0) through the near-surface dissipation. In the remaining part of this article, in the interest of brevity J will be called the Richardson number and will be used to control the stability regime.

2.2 | Inner scales and turning points

According to many articles about turbulent flows over gentle hills, it is often necessary to separate in the analysis three different layers separated by the inner layer scale and the turning level defined in Equations 1 and 2 respectively (Belcher & Wood, 1996). If we replace L by the horizontal wave number k^{-1} and take for the eddy diffusivity acting on disturbances $\nu' = 2\Lambda u_*$, Equation (1) becomes

$$kU_0(\delta) \approx \frac{2\Lambda(\delta)u_*}{\delta^2}. \tag{17}$$

We have verified that it is very well approximated by

$$\delta(k) = \left(\frac{\lambda^2}{k}\right)^{1/3}, \tag{18}$$

an expression that facilitates the asymptotic development as a function of the small parameter λ/L presented in the Appendix. The turning points are often located above the inner layer scale, at a height h_t defined by Equation (2), again replacing L by k^{-1}. Their presence quantifies wave trapping, whereas the parameter J quantifies the depth over which trapping occurs. To illustrate these points, here and in the rest of the article we will consider Gaussian ridges with characteristic horizontal scale L:

$$h(x) = H\ \mathrm{e}^{-x^2/2L^2}, \tag{19}$$

where H is the maximum mountain height. For such a profile, a large fraction of the excited harmonics have wave numbers that span the interval $2^{1/2}/L < k < 2^{-1/2}/L$. The corresponding interval in δ is shown in Figure 1b, illustrating that the inner layer scales satisfy $\lambda < \delta(k) < d$. In Figure 1c, this band of inner layer scales is also shown following the mountain profiles.

Figure 1c shows the vertical space spanned by the turning points h_t, and for the cases with $d = \infty$ (blue) and $d = L$ (red) after implicit resolution of Equation (2) and replacing $1/L$ by $2^{1/2}/L < k < 2^{-1/2}/L$ again. As in Lott et al. (2020b), one sees that in the constant-shear case ($d = \infty$, blue vertical lines) the parameter J controls the altitude of the turning levels: when $J < 1$ ($J > 1$) the turning layer is predominantly below (above) $L = 1$ km and we can expect a neutral (stratified) behaviour. Note also that using the linear–log profiles for U_V and B_V derived from the more classical Blackadar formula, Equation (8), the aforementioned diagnostics of inner layer and turning points do not differ much quantitatively.

In the variable-shear case with $d = L$ (red vertical lines), the turning points' altitude also increases with J but is located significantly higher than when $d = \infty$. Furthermore, when J approaches 1 and becomes larger, there are not many waves trapped (there is almost no turning level for $J = 2$). In these cases with fixed $d = L$, the fraction of propagating versus trapped waves is measured by comparing the Scorer parameter in the far field with $1/L^2$,

$$S_c(\infty) \gtrless 1/L^2 \Longleftrightarrow F = \frac{N(\infty)L}{U(\infty)} = \sqrt{J}\frac{L}{d} \gtrless 1,$$

where we have used the buoyancy profile in Equation (10) and the wind profile in Equation (11). F is a conventional Froude number, controlling the amount of drag that can be transported by gravity waves in the far field (Teixeira et al., 2013b). It is very likely that it impacts the surface drag, an effect that we will only measure indirectly here and by comparing the cases $\mathrm{Fr} = \sqrt{J}$ with cases with $\mathrm{Fr} = 0$ (constant shear) and $\mathrm{Fr} = \infty$ (hydrostatic). In other words, when $d = L$ we have to keep in mind that J controls both the depth of the trapping region and the significance of trapping. In this article we emphasize the first aspect and leave to a subsequent article a more systematic analysis where both the depth of the trapping region and the amount of trapping change separately.

2.3 | Non-dimensional formulation

To integrate our equations using boundary-layer techniques we start by deriving a non-dimensional form of Equations 4a–4d using the scalings

$$\begin{aligned} (X,Z) &= L\left(\overline{X},\overline{Z}\right),\\ (U_0,u,w,\mathrm{W}) &= \frac{u_* L}{\lambda}(\overline{U},\overline{u},\overline{w},\overline{\mathrm{W}}),\\ p &= u_*^2\frac{L^2}{\lambda^2}\overline{p},\\ (B_0,b) &= u_*^2\frac{L}{\lambda^2}(\overline{B},\overline{b}). \end{aligned} \tag{20}$$

All the length scales characterizing the boundary-layer depth and turbulent mixing become

$$\begin{aligned} d = L\overline{d},\quad \delta = L\overline{\delta},\quad h_t = L\overline{h}_t,\\ \lambda = L\overline{\lambda},\quad z_0 = L\overline{z}_0,\quad \Lambda_0 = \lambda\overline{\Lambda}. \end{aligned} \tag{21}$$

According to Equation (9), the last scaling makes $\overline{\Lambda}(\overline{z}) \approx O(1)$, which permits one to write Equations 4a–4d as

$$\begin{aligned} \rho\left(\overline{u}\partial_{\overline{X}}\overline{u} + \overline{\mathrm{W}}\partial_{\overline{Z}}\overline{u}\right) = -\left(\partial_{\overline{X}}\rho\overline{p} + \partial_{\overline{Z}}\rho g_{12}\overline{p}\right)\\ + \overline{\lambda}^2\partial_{\overline{Z}}\left(\overline{\Lambda}^2\|\partial_{\overline{Z}}\overline{u}\|\partial_{\overline{Z}}\overline{u}\right), \end{aligned} \tag{22a}$$

$$\begin{aligned} &\rho\left(\overline{u}\partial_{\overline{X}}\overline{w} + \overline{\mathrm{W}}\partial_{\overline{Z}}\overline{w}\right)\\ &\quad = -\partial_{\overline{Z}}\overline{p} + \rho\overline{b} + \overline{\lambda}^2\partial_{\overline{Z}}\left(\overline{\Lambda}^2\|\partial_{\overline{Z}}\overline{u}\|\partial_{\overline{Z}}\overline{w}\right), \end{aligned} \tag{22b}$$

$$\rho\left(\overline{u}\partial_{\overline{X}}\overline{b} + \overline{\mathrm{W}}\partial_{\overline{Z}}\overline{b}\right) = \overline{\lambda}^2\partial_{\overline{Z}}\left(\overline{\Lambda}^2\|\partial_{\overline{Z}}\overline{u}\|\partial_{\overline{Z}}\overline{b}\right), \tag{22c}$$

$$\partial_{\overline{X}}\rho\overline{u} + \partial_{\overline{Z}}\rho\overline{\mathrm{W}} = 0 \tag{22d}$$

and makes explicit that the small parameter controlling the inner layer dynamics is $\overline{\lambda}^2$. Still in non-dimensional form, the coordinate transform in Equation (3) writes

$$\overline{x} = \overline{X},\quad \overline{z} = \overline{Z} + \overline{h}(\overline{X})f(\overline{Z}) = \overline{Z} + \overline{z}'. \tag{23}$$

The following choice is made for the low hill and the vertical scaling function:

$$\overline{h}(\overline{x}) = S\,\mathrm{e}^{-\overline{x}^2/2} \quad\text{and}\quad f(\overline{Z}) = \exp\left(-\overline{Z}^3/3\right), \tag{24}$$

where $S = H/L$ is the mountain slope. In Equation (24), the definition of $f(\overline{Z})$ is such that, at the surface, $f(0) = 1$, $\dot{f}(0) = 0$, and $\ddot{f}(0) = 0$, properties that permit one to simplify the formalism in the inner layer.

2.4 | Linear analysis

If we consider hills of small slope S, we can assume that the response to the forcing terms is linear and consider solutions of the form

$$\begin{aligned} &\overline{u} = \overline{U} + \overline{u}',\quad \overline{w} = \overline{w}';\overline{\mathrm{W}} = \overline{\mathrm{W}}',\quad \overline{p} = \overline{P} + \overline{p}',\\ &\overline{b} = \overline{B} + \overline{b}',\quad \overline{z} = \overline{Z} + \overline{z}',\quad \rho = 1 + \rho' \end{aligned} \tag{25}$$

with normalized backgrounds

$$\overline{U}(\overline{Z}) = \overline{d}\tanh\left\{\frac{\overline{\lambda}}{\kappa\overline{d}}\log\left[\frac{\sinh\kappa(\overline{Z}+\overline{z}_0)/\overline{\lambda}}{\sinh\kappa\overline{z}_0/\overline{\lambda}}\right]\right\}, \tag{26a}$$

$$\overline{B}_{\overline{Z}} = J\coth[\kappa(\overline{Z}+\overline{z}_0)/\overline{\lambda}], \tag{26b}$$

$$\overline{\Lambda}(\overline{Z}) = \tanh[\kappa(\overline{Z}+\overline{z}_0)/\overline{\lambda}]. \tag{26c}$$

We then search solutions in the form of Fourier transforms:

$$\overline{u}'(\overline{X},\overline{Z}) = \int_{-\infty}^{+\infty}\overline{\mathbf{u}}(\overline{k},\overline{Z})\,\mathrm{e}^{\mathrm{i}\overline{k}\,\overline{X}}\,d\overline{k}. \tag{27}$$

Denoting $\overline{\boldsymbol{\rho}}$ and $\overline{\mathbf{z}}$ the Fourier transforms of ρ' and $\overline{z}'$ defined in Equation (25), Equations 22a–22d linearize to

$$\mathrm{i}\overline{k}\,\overline{U}\,\overline{\mathbf{u}} + \overline{U}_{\overline{Z}}\overline{\mathbf{W}} + \mathrm{i}\overline{k}\,\overline{\mathbf{p}} - \overline{\lambda}^2\partial_{\overline{Z}}2\overline{\Lambda}\partial_{\overline{Z}}\overline{\mathbf{u}} = \mathrm{i}\overline{k}B\overline{\mathbf{z}} \tag{28a}$$

$$\mathrm{i}\overline{k}\,\overline{U}\,\overline{\mathbf{W}} + \partial_{\overline{Z}}\overline{\mathbf{p}} - \overline{\mathbf{b}} - \overline{\lambda}^2\partial_{\overline{Z}}\overline{\Lambda}\partial_{\overline{Z}}\overline{\mathbf{w}} = \overline{\boldsymbol{\rho}}\,\overline{B} + \overline{k}^2\overline{U}^2\overline{\mathbf{z}}, \tag{28b}$$

$$\mathrm{i}\overline{k}\,\overline{U}\,\overline{\mathbf{b}} + \overline{B}_{\overline{Z}}\overline{\mathbf{W}} - \lambda^2\partial_{\overline{Z}}\left(\overline{\Lambda}\partial_{\overline{Z}}\overline{\mathbf{b}} + J\overline{\Lambda}\partial_{\overline{Z}}\overline{\mathbf{u}}\right) = 0, \tag{28c}$$

$$\mathrm{i}\overline{k}\,\overline{\mathbf{u}} + \partial_{\overline{Z}}\overline{\mathbf{W}} = -\mathrm{i}\overline{k}\,\overline{U}\,\overline{\boldsymbol{\rho}}, \tag{28d}$$

where

$$\overline{\mathbf{W}} - \overline{\mathbf{w}} = -\mathrm{i}\overline{k}\,\overline{U}\,\overline{\mathbf{z}}. \tag{28e}$$

The no-slip boundary condition become

$$\overline{\mathbf{u}}(0) = \overline{\mathbf{W}}(0) = \overline{\mathbf{b}}(0) = 0. \tag{29}$$

2.5 | Rationale of the theoretical model and relation with earlier studies

As expected with terrain-following coordinates, Equations 28a–28d contain forcing terms associated with the metric, all of which are placed at the right-hand side. In Appendix A.1 we compute the solutions of the homogeneous Equations 28a–28d, and in Appendix A.2 we compute a particular solution that equilibrates these forcings. Both solutions are used to formulate a complete solution that matches the boundary conditions. For both the homogeneous solution and the particular solution we separate the domain of integration between an "inner layer" and an "outer layer", separated by a matching region where we derive asymptotic solutions that are valid in the lower part of the outer layer and upper part of the inner layer. The homogeneous and particular solutions have exact analytical solutions in both the outer and matching regions, the solutions in the inner layer being evaluated numerically starting from solutions in the matching region. Importantly, the numerical integration starts from near 5δ down to the surface, a numerical choice that is consistent with conventional viscous boundary-layer theory where the inner layer depth, above which dissipation has less than 1% impact at leading order, is around five times the inner layer scale—see also Lott et al. (2020a), Lott et al. (2020b), and Soufflet et al. (2022).

To a large extent, Equations 28a–28d and their inner layer approximation derived in the Appendix (see Equations A26a–A26d) are similar to those in Belcher and Wood (1996), and to the basic equations in other articles using linear theory in curved coordinates (Beljaars et al., 1987; Weng et al., 1997). In terms of dynamics, there is, nevertheless, one important difference with Belcher and Wood (1996): we do not consider explicitly the presence of an almost inviscid middle layer where the Scorer parameter, Equation (2), is dominated by the background wind curvature. The reason is that our numerical integration starts from around 5δ, which corresponds to altitudes where the background wind curvature is small (in the "matching region", the background gradients are almost constant). To appreciate better the significance of the middle layer in our case, we have followed Hunt et al. (1988b) and translated those equations into a non-dimensional form and calculated the middle layer scale as the highest altitude $\overline{h}_m$ below which

$$\left\|\frac{\overline{U}_{\overline{Z}\,\overline{Z}}}{\overline{U}}\right\| \gg 1 \quad \text{and} \quad \left\|\frac{\overline{U}_{\overline{Z}\,\overline{Z}}}{\overline{U}}\right\| \gg \frac{\overline{B}_{\overline{Z}}}{\overline{U}^2} \tag{30}$$

and always found that $0 < \overline{h}_{\mathrm{m}} < 2\overline{\delta}$ with $\overline{h}_{\mathrm{m}} \approx 0$ when J is large and $\overline{h}_{\mathrm{m}} \approx 2\overline{\delta}$ when J is small (not shown). The middle layer scale is either near the inner layer scale or it does not even exist—for cases when $\overline{h}_{\mathrm{m}} < \overline{\delta}$, see Hunt et al. (1988b). This is in contrast to the altitude of the turning levels, which are often well above $\overline{\delta}$ when $J \neq 0$ (see Figure 1c). In other words, our model potentially presents a large region between the inner scale and the turning points that can support the vertical propagation of internal gravity waves; these waves will fully interact with the turning levels and the inner layer, yielding trapped lee waves that gradually attenuate downstream. This plus the intrinsic interest of providing uniform approximations are the major originalities of our work. Apart from these, our model is consistent with the truncated mixing-length model for turbulence adopted in the theory exposed in Belcher and Wood (1996) because it neglects the impact of turbulence above the inner layer consistent with the rapid-distortion mechanism.

3 | WAVE FIELD AND TRANSITION FROM DOWNSTREAM SHELTERING TO UPSTREAM BLOCKING

3.1 | Wave field

To construct the solutions of Equations 27 and 28a–28d, we consider a very large periodic domain in the horizontal (e.g., $-50 < \overline{X} < 50$) sampled by 1024 points, yielding a spectral resolution $d\overline{k} \approx 0.06$. The resolution in the vertical is refined near the surface when needed; typically, we set $d\overline{Z} \approx S/10$ near the surface (actually more for plotting purposes rather than for precision). Indeed, the solutions derived in the Appendix are analytical in the outer and matching regions (see Equations A5–A13–A16 for the homogeneous solution and Equations A24 and A25 for the particular solution). Hence, when the numerical integrations are carried out in the inner layer (Appendix A.1.3 for the homogeneous solution and Appendix A.2.3 for the particular solution) we use an adaptive vertical step to minimize the error. After being evaluated on the curved grid, the solutions are linearly interpolated on the rectangular grid, the vertical velocity $\overline{w}'$ being expressed out of $\overline{\mathrm{W}}'$ according to Equation (28e). In all panels representing the velocity fields, we take for parameter values those listed in Equation (12) and slope $S = 0.2$, their non-dimensional counterparts being given in the caption of Figure 2. Note that we will also systematically vary the non-dimensional turbulent lengths $\overline{\lambda}$ and $\overline{z}_0$ to test the sensitivity of our results to these two parameters.

We plot in Figure 2 the vertical velocity field $\overline{w}'$ when the outer flow has variable shear (Figure 2a,d,g), constant shear (Figure 2b,e,h), and variable shear with the hydrostatic approximation (Figure 2c,f,i). In each case, we present results for increasing values of the Richardson number (from top to bottom). In Figure 2a,d,g, harmonics with wave number $\overline{k} > \sqrt{J}$ encounter a turning height above which they are evanescent (see Equations A5 and A6 when $\overline{d} = 1$). In Figure 2b,e,h, all harmonics encounter

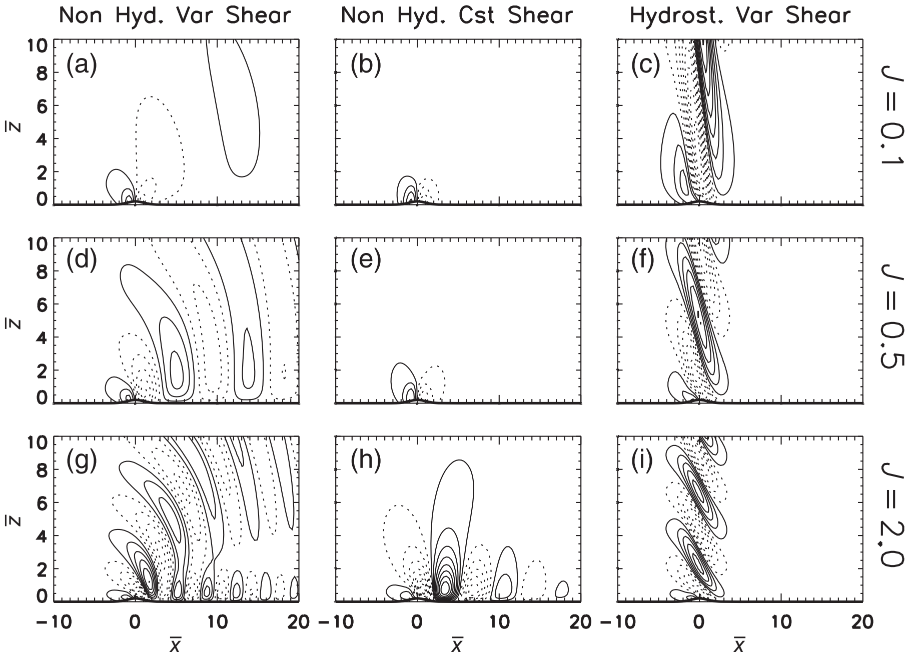

FIGURE 2 Non-dimensional vertical velocity field $\overline{w}'$ for a mountain of slope $S = 0.2$, and boundary-layer flow with mixing length $\overline{\lambda} = 0.02$ (corresponding inner layer $\overline{\delta} \approx 0.07$) and roughness length $\overline{z}_0 = 0.001$ (depth of the critical layer $\overline{z}_a \approx 0.16$). The boundary-layer depth $\overline{d} = 1$ except in (b), (e), and (h), where $\overline{d} = \infty$. Contour interval is 0.01, with negative values dashed. Note that all these patterns have been validated with the nonlinear model used in Lott et al. (2020b) (not shown).

a turning height. In Figure 2c,f,i, there is no turning point: all harmonics propagate upward when $\overline{z} \to \infty$.

A first interesting aspect to notice is that the typical amplitude of the vertical velocity right on the windward side of the hill is near $\overline{U}(\overline{\delta}/2)S \approx 0.04$, which is the amplitude of the vertical velocity produced when an inviscid flow of speed $\overline{U}(\overline{\delta}/2)$ passes over a ridge of slope S (note that the contour interval in each panel stays the same at 0.01). This situation is very similar to the constant-viscosity case discussed in Lott et al. (2020a), where dissipative effects force streamlines, up to $\overline{Z} = \overline{\delta}/2$, to be displaced vertically over a distance S, such that at $\overline{Z} = \overline{\delta}/2$ the vertical velocity should scale as $\overline{U}(\overline{\delta}/2)S$.

If we now look for similarities with previous constant-viscosity studies, we conclude that the solutions with variable wind in Figure 2a,d,g are similar to those shown in Soufflet et al. (2022). In the near-neutral case (Figure 2a) almost no waves develop aloft because most harmonics encounter a turning height and perhaps because the resonant modes have longer horizontal wavelength than those predominantly excited by Equation (19)—as in Soufflet et al. (2022) and anticipating results in a subsequent article. In contrast, when $J = 0.5$ in Figure 2d, trapped waves dominate the response, because many harmonics still encounter turning altitudes, whereas near-resonant modes have shorter horizontal wavelength. The response becomes dominated by upward propagating waves when $J = 2$ in Figure 2g. This occurs because less harmonics encounter turning height, but there is also a system of trapped lee waves developing downstream.

The solutions with constant shear in Figure 2b,e,h are characterized by very weak waves up to $J = 0.5$ (Figure 2b,e), which is a consequence of the facts that (i) all harmonics encounter turning heights in the vertical, (ii) the turning heights are located near the surface (around $\overline{h}_t \approx \sqrt{J}$), and (iii) upward waves cannot fully develop. When J increases further in Figure 2h, trapped lee waves start to develop. They have two origins, the first is that in this case the gravity waves have more room to propagate vertically before returning to the surface downstream (see Lott et al., 2020b), and the second is that the waves returning to the surface are less absorbed than in the constant-viscosity case, permitting downward propagation. A more complete analysis of the trapped waves will be given in a subsequent article, but the onset of trapped waves when the wind shear becomes constant is reminiscent of the inviscid solutions with constant wind shear and non-zero wind at the surface in Keller (1994).

The hydrostatic solutions in Figure 2c,f,i present purely vertically propagating waves, as expected from Equation (A7), the vertical wavelength decreasing with J.

3.2 | Downstream sheltering versus upstream blocking

To characterize the near-surface flow, we plot in Figure 3 the wind perturbation caused by the hill, normalized by the incident wind and the total wind vector (background plus perturbation) in the quasi-neutral and stratified cases shown in Figure 2a,g. The neutral case in Figure 3a shows a relative augmentation in wind amplitude above the hill top compared with the upstream

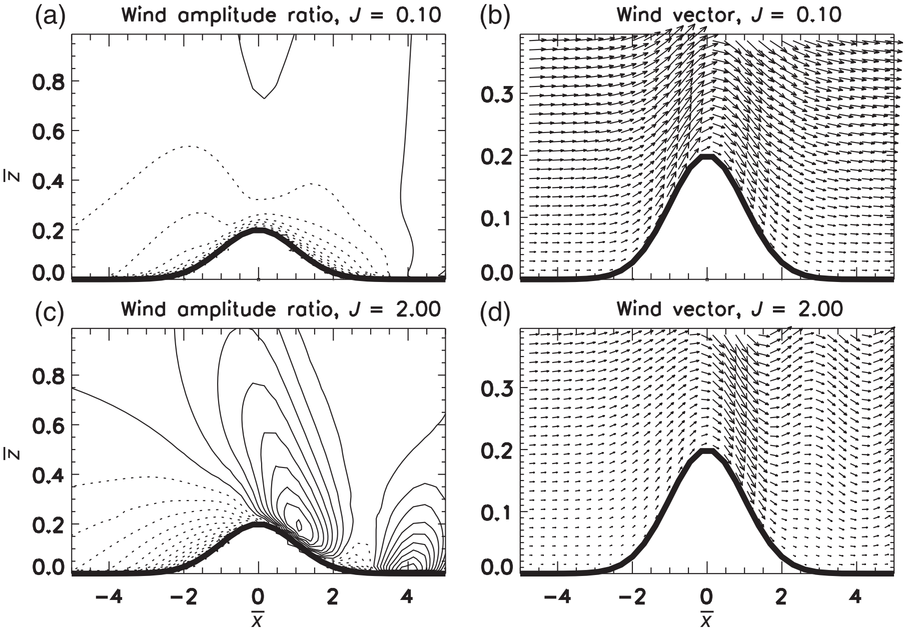

FIGURE 3 Near-mountain velocity fields with the same parameters as in Figure 2b,h. (a, c) The total wind amplitude normalized by the background wind, $\sqrt{\overline{u}^2+\overline{w}^2}/\overline{U}(Z)$. The contour interval is 0.1 with values below zero dashed. (b, d) The total wind vector $\overline{u}, \overline{w}$.

flank, and an intensification above the hill crest that is characteristic of neutral flow over hills. Still in the near-neutral case, the wind amplitude along the downstream flank is also reduced compared with the upstream flank, a behaviour characterizing non-separated sheltering and produced by enhanced surface friction and dissipation as the air travels across the ridge. Note, nevertheless, that the sheltering effect is much less pronounced than in the constant-viscosity case, a behaviour that naturally follows from the decrease of the diffusion coefficient when approaching the surface—compare Figure 3b here and Lott et al. (2020b, fig. 6b).

In the stratified case in Figure 3c,d, the upslope/-downslope asymmetry is much more pronounced: there is strong wind intensification on the downstream side, with strong downslope winds penetrating well into the inner layer. On the upstream side there is also pronounced deceleration, a process that we called non-separated blocking in Lott et al. (2020b).

We analyse more systematically the transition from neutral to stratified flow according to the downslope/upslope asymmetry—that is, following Soufflet et al. (2022)—in Figure 4. We plot the ratio between the downslope wind intensity and upslope wind intensity,

$$\underbrace{Max}_{\overline{z}<\frac{2S}{3},0<\overline{x}<2} \sqrt{\overline{u}^2+\overline{w}^2} \Big/ \underbrace{Max}_{\overline{z}<\frac{2S}{3},-2<\overline{x}<0} \sqrt{\overline{u}^2+\overline{w}^2}, \tag{31}$$

as a function of the Richardson number J. We also systematically vary the value of the mixing length $\overline{\lambda}$ between 0.005 and 0.05, a range of variation that permits one to satisfy $\overline{\delta} \ll 1$ and to keep the dimensional values of λ of the order

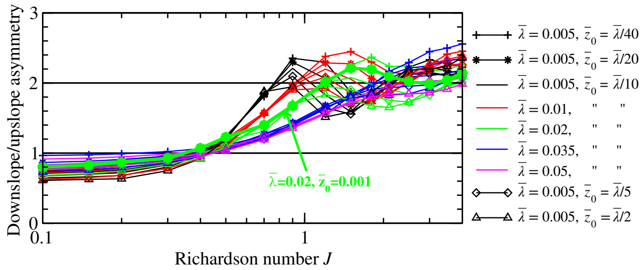

FIGURE 4 Downslope sheltering versus upstream blocking index defined as the ratio between the maximum downslope wind amplitude and the maximum upslope wind amplitude; see Equation (31). Non-hydrostatic cases with variable shears, $S = 0.2$, and for values of $\overline{\lambda}$ and $\overline{z}_0$ shown in the legend.

of 20 m and below when the the dimensional hill length varies in the range 200 m < L < 5 km. In order to be consistent with our asymptotic analysis, we have to keep the roughness length $\overline{\lambda}/2 < \overline{z}_0 < \overline{\lambda}/40$, and to keep $\overline{z}_a = O(\overline{\delta})$, $\overline{z}_a$ being controlled by the ratio $\overline{z}_0/\overline{\lambda}$; see Equation (14). Physically, this means that our calculations are only valid if the depth of the critical level $\overline{z}_a$ compares with the inner layer scale. In practice, we found that we should always satisfy the criterion $5\overline{\delta} - \overline{z}_a > 0$ to have inner solutions that converge.

For almost all values of the dissipation parameters, Figure 4 shows that the transition from neutral to stratified behaviour occurs for $J \approx 0.5$, almost as in Soufflet et al. (2022, fig. 7b). The sheltering is nevertheless less pronounced, the ratio in Equation (31) falling below 0.5 in the constant-viscosity case when $J \ll 1$ and for $S = 0.15$, whereas it is always between 0.5 and 1 for a larger slope

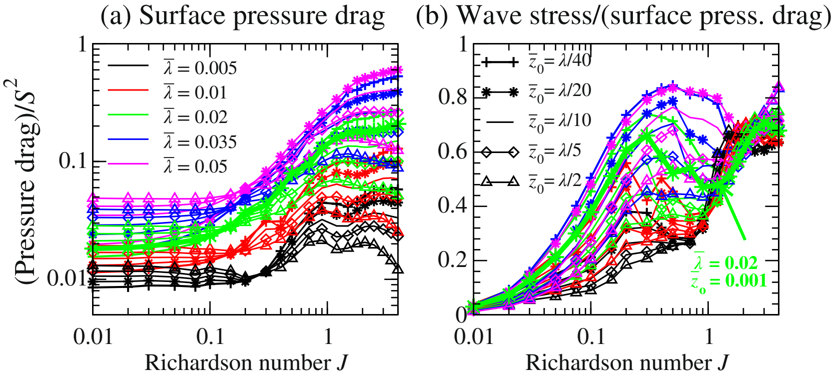

FIGURE 5 Mountain drag and wave momentum flux divided by S^2 in the non-hydrostatic variable-shear case and for different values of $\bar{\lambda}$ and $\bar{z}_0$. (a) Mountain drag $\overline{\overline{\tau}}_{\text{wav}}(\overline{Z} = 0)$. (b) Ratio between wave stress in the far field and at the mountain drag, $\overline{\overline{\tau}}_{\text{wav}}(\overline{Z} = \infty)/\overline{\overline{\tau}}_{\text{wav}}(\overline{Z} = 0)$.

($S = 0.2$). Again, this is related to the fact that, here, dissipative effects are smaller near the surface when compared with the constant-viscosity case.

4 | WAVES STRESS AND MOUNTAIN DRAG

4.1 | Pressure drag and momentum fluxes

To appreciate the action of the wave on the large-scale flow, we next use a momentum budget in curved coordinates by averaging in $\overline{X}$ Equation (22a) written in flux form,

$$\frac{\partial \overline{\rho\overline{\overline{u}}}}{\partial \bar{t}} = \frac{\partial}{\partial Z}\left(\underbrace{\overline{-\rho\bar{u}\,\overline{\overline{\mathrm{W}}}} + \overline{\bar{p}\partial_{\overline{X}}\bar{z}}}_{\overline{\overline{\tau}}_{\text{wav}}} + \overline{\overline{\tau}}_{\overline{X}\,\overline{Z}}\right), \tag{32}$$

where we have "re-"introduced a "large-scale" tendency on the left-hand side to emphasize that we will use the stationary linear model to analyse the effect of the disturbances on the large-scale flow. This expression is appealing because the first two terms in the momentum flux on the right-hand side permit one to capture smoothly the transition from mountain drag at $Z = 0$ to the conventional "Eulerian mean" wave momentum flux when $\overline{Z} \gg 1$ (e.g., where $\overline{Z} = \bar{z}$). To a certain extent this expression also has a Lagrangian character. In the surface layer, the averaging is simply along the streamlines that follow the ridge, making the average in good part Lagrangian by construction. Above the inner layer it follows that, when dissipation is weak, the Reynolds stress alone equals the pressure torque along streamlines—see Lott et al. (2020a, eq. 23) when dissipation is small. In the following, we analyse the wave stress $\overline{\overline{\tau}}_{\text{wav}}$, which is the contribution of our linear solutions to the sum of these two terms, after verification that the second-order contribution to the dissipative stress $\overline{\overline{\tau}}_{\overline{X}\,\overline{Z}}$, $(\bar{\lambda}\,\overline{\Lambda}\bar{u}'_{\overline{Z}})^2$, is significantly smaller than the wave stress in the inner layer.

Figure 5a shows the surface pressure drag as a function of J in the variable-shear case ($\bar{d} = 1$) and for the different values of the parameters $\bar{\lambda}$ and $\bar{z}_0$. The pressure drag is divided by S^2, simply because we diagnose a quadratic term from a theory that is linear in S. On it, we see that the curves spread over a very large range of values and that the drag has a systematic tendency to increase with J. This is the classical behaviour where gravity wave drag gradually replaces the form drag due to non-separated sheltering and when the trapping region becomes thicker (Yu & Teixeira, 2015). There is also a tendency for the drag to increase with $\bar{\lambda}$. As the incident wind at the inner layer scale $\overline{U}(\bar{\delta})$ increases with $-\lambda$ (not shown), this is consistent with our results in Lott et al. (2020a), where we show that it is the incident wind at the inner layer scale that controls the drag amplitude.

The dependence of the drag on $\bar{z}_0$ is related to flow stability. In the neutral case, say for $J < 0.5$, the drag increases with roughness ("triangles" are above "plus signs") simply because there is more dissipation, making the sheltering more pronounced ("triangles" are below "plus signs" in Figure 4). The situation reverses in the stratified case ($J > 0.5$), where the drag decreases when the roughness length increases. An interpretation could be that when there is an increase in $\bar{z}_0$ then $\bar{z}_a$ decreases; that is, the critical level gets closer to the surface, which makes the waves become more attenuated by the enhancement of the dissipative effects that occur near critical levels (Booker & Bretherton, 1967). As in these cases the drag is dominated by wave drag, enhanced wave dissipation could result in decreased wave drag.

Figure 5b plots the ratio between the wave stress in the far field and the surface pressure drag. Without a surprise, one sees that for small J, most of the pressure drag is deposited at low levels (typically about 80% when $J \leq 0.1$), which is a natural consequence of the fact that most harmonics are evanescent in the vertical and in the far field. At the other extreme for the stable cases, a good fraction of

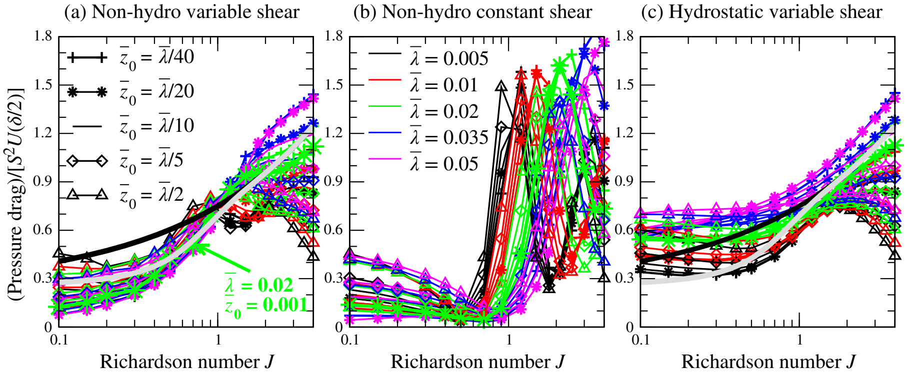
(a) Non-hydro variable shear

(b) Non-hydro constant shear

(c) Hydrostatic variable shear

FIGURE 6 Mountain drag divided by $S^2\overline{U}(\delta/2)$ and for different values of $\bar{\lambda}$ and $\bar{z}_0$. The thick black and grey lines in (a) and (c) are for the rough estimates of the variations in drag with Richardson number discussed in Section 5 (see Equations 33 and 34 respectively).

the drag radiates in the far field (about 70% when $J > 1$), with only 30% of the surface drag being eroded by dissipation. Finally, the transition region, say for $0.1 < J < 1$, is remarkably rich in terms of variations in this ratio. When we look at the vertical velocity fields in Figure 2 and compare the case with $J = 0.5$ in Figure 2e with the other less stable and more stable cases in Figure 2b,h respectively, we see that the transition region is clearly dominated by trapped lee waves that do not contribute substantially to the momentum flux in the far field. In this intermediate regime, we also observe a big variability in the momentum flux arriving in the far field. As an illustration, we see in Figure 5b that, for $J = 0.3$, about 20% of the drag becomes a momentum flux when ($\bar{\lambda} = 0.005, \bar{z}_0 = \bar{\lambda}/2$) (black line with triangles), whereas it is 80% when ($\bar{\lambda} = 0.035, \bar{z}_0 = \bar{\lambda}/10$) (blue line with diamonds).

Following the earlier suggestion that the incident velocity relevant for the drag must be measured at the inner layer scale, Figure 6a shows the pressure drag divided by $\overline{U}(\bar{\delta}/2)S^2$, which is an estimate of the wave drag occurring for an incident flow of speed $\overline{U}(\bar{\delta}/2)S^2$ when $J = 1$. We believe that this predictor could also work for the drag due to non-separated sheltering because it compares relatively well with $\bar{\delta}\,\overline{u}(S)S$, a measure of the drag associated with the pressure decrease across the hill that equilibrates surface friction (see Lott et al., 2020b). With this normalization, one sees that the drag values remain on the order of magnitudes around 1, with smaller values in the neutral cases and larger values in the stratified cases. The figure also illustrates well the transition around $J = 1$, with larger drag in the stratified case. There is, nevertheless, a rich variability in drag as a function of $\bar{z}_0$ and $\bar{\lambda}$ when stability is large; we did not manage to capture this variability with a simple predictor.

To emphasize the significance of the conditions of wave propagation aloft, we plot in Figure 6b,c the drag when all the waves are trapped (the non-hydrostatic case with constant shear) and free to propagate aloft (hydrostatic with variable shear). When all the disturbances are trapped in Figure 6b, the transition at $J \approx 1$ is even more pronounced than in Figure 6a. In almost all cases, and when J varies between 0.5 and 1, the drag decreases before increasing rapidly as J approaches 1. These rapid transitions occur for all values of $\bar{\lambda}$ and $\bar{z}_0$, as was also seen in the constant-viscosity case. This variation is related to the interaction between the reflected waves and the surface (yielding relatively low and high drag states also see Teixeira et al., (2013a). When all the waves can propagate aloft, we observe the opposite behaviour (Figure 6c, hydrostatic variable shear). The variations in drag with J are much less dramatic than in the other two cases. Interestingly, one sees that for small J the pressure drag is larger than in Figure 6a,b, illustrating that allowing all the disturbances to propagate freely as gravity waves in the vertical direction favours the drag. Of course, this is academic, since only few disturbances can propagate vertically when J is small in the non-hydrostatic case, but it illustrates the general significance of the waves for the mountain drag.

Finally, Figure 7 shows vertical profiles of the waves stress ($\bar{\tau}_{\rm wav}$ in Equation 32) in the nine cases presented in Figure 2. As expected, we see a decrease with altitude of the momentum flux, which typically occurs over a depth near $\overline{Z} \approx 3\bar{\delta} \approx 0.2$. The fact that such a decrease occurs inside the inner layer depth $5\bar{\delta}$ is systematic, but the exact depth is somehow dependent on the critical level depth $\bar{z}_a$ (and hence $\bar{z}_0$) (not shown). We see that the momentum flux decrease has two causes: (i) the effect of wave trapping that always dominates the constant-shear case (black curves) and (ii) the erosion by dissipation of the waves when they travel upward through the inner layer and that is the only mechanism at work in the hydrostatic case (about 15%–20% erosion, see blue curves). In the non-hydrostatic case with variable shear, one sees that the two effects contribute almost equally. For instance, in the stratified case ($J = 2$), the red and blue dotted curves show that the decrease of the stress in the inner layer is two to three times larger in the non-hydrostatic case than in the hydrostatic one. The contribution of the trapped waves to the momentum flux decay equals and exceeds the erosion of the freely propagating waves.

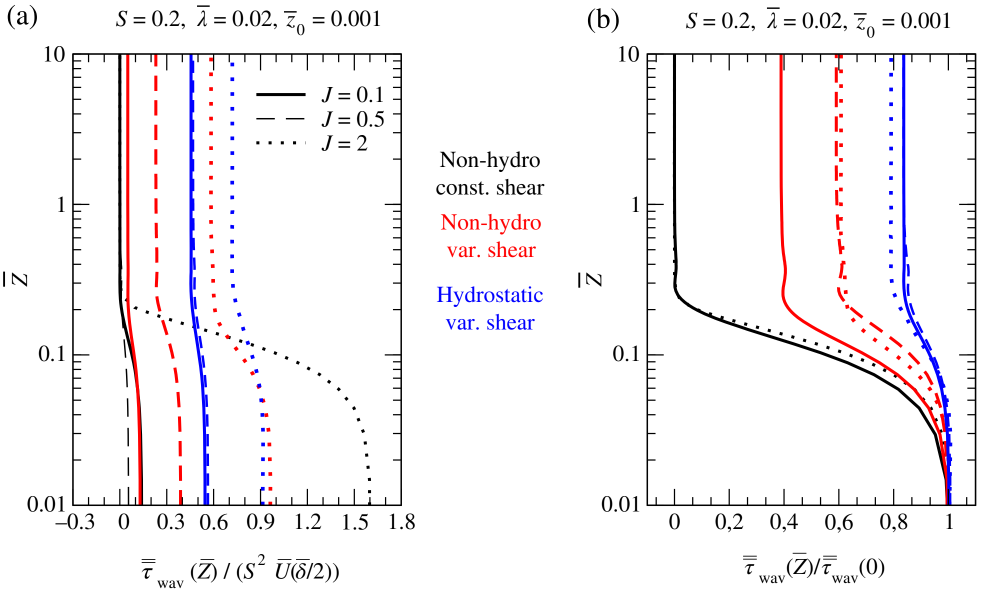

FIGURE 7 Momentum flux vertical profiles according to Equation 32 and for the nine cases in Figure 2. Panels on the left and right are identical except the stress profiles in (b) are divided by the surface value to emphasize erosion with altitude.

5 | SUMMARY AND DISCUSSION

In dynamical meteorology and oceanography, boundary-layer turbulence is often parametrized with an eddy diffusivity in order to capture the interaction between the surface and the boundary layer. Although these types of closure are today questioned—for instance, because the smallest scales of turbulence can backscatter on the large scales (Schumann & Launder, 1995; Weinbrecht & Mason, 2008), or in mountainous areas because the turbulence is notoriously non-homogeneous in the horizontal direction (Stiperski & Rotach, 2016)—many numerical models still use them. It seems essential, therefore, to provide theory that could help explain the behaviour of these models; for example, the system of mountain waves developing in a boundary layer parametrized by a classical mixing-length closure.

This type of study could also provide some guidance to develop parametrization of subgrid-scale orography for at least two reasons. The first is that parametrizations of subgrid-scale mountains are rooted in linear theories that depict (i) the interaction between the boundary layer and subgrid-scale orography using eddy diffusivity closure, and (ii) the generation of mountain waves in the stratified case neglecting the boundary layer (except that the large-scale flow that enters in the evaluation of the wave drag is impacted by the boundary layer). The second is that the transition between stratified and neutral flow can seemingly be characterized by near-resonant trapped lee waves that are not well parametrized in models. This article provides some answers to help in developing a parametrization that encompasses all the scales of the SSO. The first answer is that it suggests that the incident wind value at the inner layer scale should be used to measure the drag (or average over the inner layer; see normalization in Figure 6). In a large-scale model that uses a viscosity-type closure, and for a given mountain length, this height can be diagnosed by comparing the amplitude of the disturbance advection with dissipation—according to Equation (1). With our mixing-length model closure this is well approximated by $\delta = L^{1/3}\lambda^{2/3}$, as in Equation (18) with $k = 1/L$. The second answer is that the nature of the drag (i.e., mountain drag due to non-separated sheltering versus gravity wave drag) has to be decided above the inner layer. This is very important because it can be done without requesting information about the properties of the turbulence itself; we just have to find, for a given mountain length L, the turning point altitude h_t, defined in Equation (2), and compare it with L. If $h_t < L$, gravity waves do not have enough space to develop in the vertical and the dynamics is neutral, if $h_t > L$ then the dynamics is stratified. More specifically, in the constant-shear cases with the turning altitude at around $h_t \approx \sqrt{J}L$, small (large) values of J mean that the turning altitude is close to the surface (far from the surface) and we found neutral (stratified) behaviour. In the variable-shear case, the turning altitude is slightly above the surface for small J and substantially higher (up to the top of the atmosphere) for large J, yielding about the same qualitative conclusions. In contrast to Belcher and Wood (1996), we find that this turning altitude should not be used to evaluate the incident wind that enters in the drag formula.

Making closed-form predictions beyond the fact that the drag scales with

$$\rho_s\left[\frac{u_* L}{\lambda} U(\delta/2) S^2\right]$$

turned out to be quite difficult, so we did not propose any in the core of the article. Nevertheless, we can suggest some attempts to capture at least the J dependence. The first is

$$\left[\rho_s \frac{u_* L}{\lambda} U(\delta/2) S^2\right] 0.25 \times (1 + 2\sqrt{J}), \tag{33}$$

where the first term in brackets is the dimensional form of the normalization used in Figure 6, and the second term is the sum of a form drag and a wave drag, as shown by the thick black curves in Figure 6a,c. This fit is adapted in the hydrostatic case when all disturbances becomes waves in the far field. It overestimates the drag in the neutral case, where gravity waves should not play a role. So, to separate both regimes and allow a rapid transition from one to the other, we also plot in thick grey the predictor

$$\left[\rho_s \frac{u_* L}{\lambda} U(\delta/2) S^2\right] \times 0.25 \times \left\{1 + \left[1 + \tanh\left(\frac{J - 0.5}{0.5}\right)\right]\sqrt{J}\right\}. \tag{34}$$

The tanh term in Equation (34) limits the wave contribution in the neutral case and allows for a quite rapid transition from the neutral to the stratified cases. The rapid increase in drag when $J \approx 0.5$ is presumably related to trapped waves.

An important limitation of our work, nevertheless, is that we have focused on the depth of the trapping region and less on the relative amount of waves that stay trapped (i.e., that are evanescent for $z \rightarrow \infty$). This relative amount is controlled by the inverse Froude number

$$F^{-1} = \frac{U(\infty)}{N(\infty)L}, \tag{35}$$

which is well known to control the non-hydrostatic effect on the mountain wave drag (Teixeira et al., 2013b). In the constant-shear case ($F^{-1} = \infty$), all the waves stay trapped; in the variable-shear case ($F^{-1} = d/(L\sqrt{J})$), the fraction of trapped waves decreases when J increases because we always take $d/L = 1$; and in the hydrostatic case ($F^{-1} \approx 0$), all the waves propagate up. Accordingly, it is likely that the increase in drag with J in Figure 6a is due to the fact that more waves can propagate up. To illustrate that this effect is at work in our results, we notice that when J is small ($J \leq 0.5$) the drag is larger in the variable-shear case than when all the waves are trapped (Figure 6b) and smaller than when all can propagate up (Figure 6a). In a companion paper, we do experiments where J only controls the free shear layer stability, not the amount of trapping; for instance, leaving F constant by taking $d = L\sqrt{J}$.

We are not going to speculate further on the application of our results, except to formulate them in a way that involves further the background flow at the dynamical levels we have identified. We can, for example, approximate the wind factor $u_* L/\lambda$ by $U(h_t)$ and we can interpret the Richardson number dependence in terms of $\overline{h}_t$, the ratio between the turning heights and the mountain length, in which case the drag predictor, Equation (33), can be roughly approximated by

$$\rho_s U(h_t) U(\delta/2) S^2 \overline{h}_c^{-2} \left(1 + \overline{h}_t/\overline{h}_c\right), \tag{36}$$

where $\overline{h}_t = h_t/L$ and $\overline{h}_c = 0.5$ is a critical value. In all these formulas one should replace $\overline{h}_t$ by the "normalized" boundary layer depth $\overline{d}$ when it is larger. This formula could be compared with Belcher and Wood (1996), the slope S being replaced by Hk and $\overline{h}_t$ by the inverse of a Froude number, $F_t^{-1} = U(h_t)/LN(h_t)$. According to the previous discussion herein concerning the potential role of the Froude numbers on the dynamics and drag, we leave this issue to further analysis. In this article, the most significant difference we identify is that one of the two background wind values in Equation (36) is to be taken near the inner layer scale (i.e., in $\delta/2$) not at the turning altitude h_t. Nevertheless, the most important similarity is that, in both formulations, the nature of the dynamics (neutral or stratified) has to be decided at the turning height.

AUTHOR CONTRIBUTIONS

Francois Lott: conceptualization; formal analysis; methodology; writing – original draft. **Anton Beljaars:** conceptualization; methodology; writing – original draft. **Lucile Pauget:** software; validation. **Bruno Deremble:** validation; writing – original draft.

ORCID

Francois Lott https://orcid.org/0000-0003-2126-5510

REFERENCES

Allen, T. & Brown, A. (2002) Large-eddy simulation of turbulent separated flow over rough hills. *Boundary-Layer Meteorology*, 102, 177–198.

Ambaum, M. & Marshall, D. (2005) The effects of stratification on flow separation. *Journal of the Atmospheric Sciences*, 62, 2618–2625.

Belcher, S.E. & Wood, N. (1996) Form and wave drag due to stably stratified turbulent flow over low ridges. *Quarterly Journal of the Royal Meteorological Society*, 122, 863–902.

Beljaars, A., Walmsley, J. & Taylor, P. (1987) A mixed spectral finite-difference model for neutrally stratified boundary-layer flow over roughness changes and topography. *Boundary-Layer Meteorology*, 38, 273–303.

Beljaars, A.C.M., Brown, A.R. & Wood, N. (2004) A new parametrization of turbulent orographic form drag. *Quarterly Journal of the Royal Meteorological Society*, 130, 1327–1347.

Boegman, L. & Stastna, M. (2019) Sediment resuspension and transport by internal solitary waves. *Annual Review of Fluid Mechanics*, 51, 129–154.

Booker, J.R. & Bretherton, F.P. (1967) The critical layer for internal gravity waves in a shear flow. *Journal of Fluid Mechanics*, 27, 102–109.

Chimonas, G. & Nappo, C.J. (1989) Wave drag in the planetary boundary layer over complex terrain. *Boundary-Layer Meteorology*, 47, 217–232.

Clark, T.L. (1977) A small-scale dynamic model using a terrain-following coordinate transformation. *Journal of Computational Physics*, 24, 186–215.

Durran, D.R. (1990) Mountain waves and downslope winds. *AMS Meteorological Monographs*, 23, 59–83.

Finnigan, J., Ayotte, K., Harman, I., Katul, G., Oldroyd, H. & Patton, E. (2020) Boundary-layer flow over complex topography. *Boundary-Layer Meteorology*, 177, 247–313.

Hunt, J.C.R., Leibovich, S. & Richards, K.J. (1988a) Turbulent shear flows over low hills. *Quarterly Journal of the Royal Meteorological Society*, 114, 1435–1470.

Hunt, J.C.R., Richards, K.J. & Brighton, P.W.M. (1988b) Stably stratified shear flow over low hills. *Quarterly Journal of the Royal Meteorological Society*, 114, 859–886.

Keller, T.L. (1994) Implications of the hydrostatic assumption on atmospheric gravity waves. *Journal of the Atmospheric Sciences*, 51, 1915–1929.

Koppel, D. (1964) On the stability of flow of a thermally stratified fluid under the action of gravity. *Journal of Mathematical Physics*, 5, 963–982.

Lott, F., Deremble, B. & Soufflet, C. (2020a) Mountain waves produced by a stratified boundary layer flow. Part I: hydrostatic case. *Journal of the Atmospheric Sciences*, 77, 1683–1697.

Lott, F., Deremble, B. & Soufflet, C. (2020b) Mountain waves produced by a stratified shear flow with a boundary layer. Part II: form drag, wave drag, and transition from downstream sheltering to upstream blocking. *Journal of the Atmospheric Sciences*, 78, 1101–1112.

Lott, F. & Miller, M. (1997) A new subgrid scale orographic drag parameterization; its testing in the ecmwf model. *Quarterly Journal of the Royal Meteorological Society*, 123, 101–127.

Palmer, T.N., Shutts, G.J. & Swinbank, R. (1986) Alleviation of systematic westerly bias in general circulation and numerical weather prediction models through an orographic gravity wave drag parametrization. *Quarterly Journal of the Royal Meteorological Society*, 112, 2056–2066.

Pokharel, B., Geerts, B., Chu, X. & Bergmaier, P. (2017) Profiling radar observations and numerical simulations of a downslope wind storm and rotor on the lee of the medicine bow mountains in Wyoming. *Atmosphere*, 8, 39.

Reinert, D., Wirth, V., Eichhorn, J. & Panhans, W.-G. (2007) A new large-eddy simulation model for simulating air flow and warm clouds above highly complex terrain. Part i: the dry model. *Boundary-Layer Meteorology*, 125, 109–132.

Richard, E., Mascart, P. & Nickerson, E.C. (1989) The role of surface friction in downslope windstorms. *Journal of Applied Meteorology*, 28, 241–251.

Ross, A., Arnold, S., Vosper, S., Mobbs, S., Dixon, N. & Robins, A. (2004) A comparison of wind tunnel experiments and simulations of neutral and stratified flow over a hill. *Boundary-Layer Meteorology: An International Journal of Physical and Biological Processes in the Atmospheric Boundary Layer*, 113, 427–459.

Sachsperger, J., Serafini, S. & Grubisic, V. (2015) *Lee waves on the boundary-layer inversion*. Frontiers in Geophysics. Submitted.

Sauer, J.A., Muñoz-Esparza, D., Canfield, J.M., Costigan, K.R., Linn, R.R. & Kim, Y.-J. (2016) A large-eddy simulation study of atmospheric boundary layer influence on stratified flows over terrain. *Journal of the Atmospheric Sciences*, 73, 2615–2632.

Schumann, U. & Launder, B.E. (1995) Stochastic backscatter of turbulence energy and scalar variance by random subgrid-scale fluxes. *Proceedings of the Royal Society of London. Series A: Mathematical and Physical Sciences*, 451, 293–318.

Smith, R.B., Jiang, Q. & Doyle, J.D. (2006) A theory of gravity wave absorption by a boundary layer. *Journal of the Atmospheric Sciences*, 63, 774–781.

Soontiens, N., Stastna, M. & Waite, M.L. (2015) Topographically generated internal waves and boundary layer instabilities. *Physics of Fluids*, 27, 086602.

Soufflet, C., Lott, F. & Deremble, B. (2022) Mountain waves produced by a stratified shear flow with a boundary layer. Part iii: trapped lee waves and horizontal momentum transport. *Journal of the Atmospheric Sciences*, 79, 1601–1614.

Stiperski, I. & Rotach, M.W. (2016) On the measurement of turbulence over complex mountainous terrain. *Boundary-Layer Meteorology*, 159, 97–121.

Sun, J. (2011) Vertical variations of mixing lengths under neutral and stable conditions during cases-99. *Journal of Applied Meteorology and Climatology*, 50, 2030–2041.

Teixeira, M.A.C., Argain, J.L. & Miranda, P.M.A. (2013a) Orographic drag associated with lee waves trapped at an inversion. *Journal of the Atmospheric Sciences*, 70, 2930–2947.

Teixeira, M.A.C., Argaín, J.L. & Miranda, P.M.A. (2013b) Drag produced by trapped lee waves and propagating mountain waves in a two-layer atmosphere. *Quarterly Journal of the Royal Meteorological Society*, 139, 964–981.

Tsiringakis, A., Steeneveld, G.-J. & Holtslag, A. (2017) Small-scale orographic gravity wave drag in stable boundary layers and its impact on synoptic systems and near-surface meteorology. *Quarterly Journal of the Royal Meteorological Society*, 143, 1504–1516.

Voigt, M. & Wirth, V. (2013) Mechanisms of banner cloud formation. *Journal of the Atmospheric Sciences*, 70, 3631–3640.

Vosper, S.B., Brown, A.R. & Webster, S. (2016) Orographic drag on islands in the nwp mountain grey zone. *Quarterly Journal of the Royal Meteorological Society*, 142, 3128–3137.

Weinbrecht, S. & Mason, P.J. (2008) Stochastic backscatter for cloud-resolving models. Part i: implementation and testing in a dry convective boundary layer. *Journal of the Atmospheric Sciences*, 65, 123–139.

Weng, W., Chan, L., Taylor, P. & Xu, D. (1997) Modelling stably stratified boundary-layer flow over low hills. *Quarterly Journal of the Royal Meteorological Society*, 123, 1841–1866.

Wieringa, J. (1992) Updating the davenport roughness classification. *Journal of Wind Engineering and Industrial Aerodynamics*, 41, 357–368 https://www.sciencedirect.com/science/article/pii/016761059290434C

Wood, N., Brown, A. & Hewer, F. (2001) Parameterizing the effects of orography on the boundary layer: an alternative to effective roughness lengths. *Quarterly Journal of the Royal Meteorological Society*, 127, 759–777.

Wood, N. & Mason, P. (1993) The pressure force induced by neutral, turbulent flow over hills. *Quarterly Journal of the Royal Meteorological Society*, 119, 1233–1267.

Yu, C.L. & Teixeira, M.C. (2015) Impact of non-hydrostatic effects and trapped lee waves on mountain-wave drag in directionally sheared flow. *Quarterly Journal of the Royal Meteorological Society*, 141, 1572–1585.

How to cite this article: Lott, F., Beljaars, A., Pauget, L. & Deremble, B. (2023) Neutral and stratified turbulent boundary-layer flow over low mountains. *Quarterly Journal of the Royal Meteorological Society*, 1–18. Available from: https://doi.org/10.1002/qj.4591

APPENDIX A. MIXED THEORETICAL FINITE-DIFFERENCE MODEL

To solve the set of Equations 28a–28d over a semi-infinite domain, we combine theoretical inviscid solutions and numerical solutions in the inner layer, with the inner layer scale varying for each harmonic according to

$$\overline{\delta}(\overline{k}) = \left(\frac{\overline{\lambda}^2}{\overline{k}}\right)^{1/3}. \tag{A1}$$

The matching between the inviscid or "outer layer" solution will be made in a matching region in which analytical asymptotic solutions are also derived. These "matching" solutions will permit one to initialize the dissipative equations at $\overline{z} \approx 5\overline{\delta}$, which is relatively near the ground, and integrate them down to the surface to give the "inner solutions". The uniform solutions are combinations of these three "outer", "matching", and "inner" solutions; they will be evaluated for both the homogeneous solution and the particular solution. The derivation of the matching solutions is central to our study, because in them one can identify those asymptoting the inviscid solution and which are the Booker and Bretherton (1967) solutions, and those with exponential growth with altitude and which are purely due to dissipations. The fact that they have exponential growth explains why the system we analyse is almost impossible to integrate numerically from $\overline{z} \approx \infty$ to the surface.

A.1 Homogeneous solution

A.1.1 Outer solution

When $\overline{\lambda} \ll 1$ and without the right-hand side terms, the set of Equations 28a–28d reduce to the homogeneous inviscid equations. We will use this approximation where $\overline{Z} \gg \overline{\delta}$; and as $\overline{\delta} > \overline{\lambda}$, they can be solved using the background profiles approximated by

$$\overline{U} \approx \overline{d} \tanh \frac{\overline{Z} + \overline{z}_{\mathrm{a}}}{\overline{d}}, \quad \overline{B} \approx J(\overline{Z} + \overline{z}_{\mathrm{a}}). \tag{A2}$$

For such profiles, the inviscid homogeneous part of Equations 28a–28d satisfies the Taylor–Goldstein equation,

$$\frac{d^2\overline{\mathbf{W}}}{d\overline{Z}^2} + \left[\frac{J}{\overline{U}^2} + \frac{2}{\overline{d}^2}\left(1 - \frac{\overline{U}^2}{\overline{d}^2}\right) - \overline{k}^2\right]\overline{\mathbf{W}} = 0, \tag{A3}$$

the solutions of which can be expressed in terms of Haenkel functions when $\overline{d} = \infty$ or hypergeometric functions when $\overline{d} \neq \infty$; that is, the solution named $\overline{\mathbf{w}}_{\mathrm{I}}$ given in Lott et al. (2020b, eq. 12) and Soufflet et al. (2022, eq. 13) respectively. The only difference with Lott et al. (2020b) and Soufflet et al. (2022) is that the critical level is at $Z = -\overline{z}_{\mathrm{a}}$ rather than at $Z = 0$, a behaviour that is transparent when we write the asymptotic forms

$$\overline{\mathbf{W}}_{\mathrm{I}}(\overline{z}) = \overline{\mathbf{w}}_{\mathrm{I}}(\overline{k}, \overline{Z} + \overline{z}_{\mathrm{a}}) \underbrace{\approx}_{\overline{Z}\to\infty} \mathrm{e}^{-\overline{m}(\overline{Z}+\overline{z}_{\mathrm{a}})}, \tag{A4}$$

$$\underbrace{\approx}_{\overline{Z}\to 0} \overline{a}_1\left(\overline{Z} + \overline{z}_{\mathrm{a}}\right)^{1/2-\mathrm{i}\mu} + \overline{a}_2\left(\overline{Z} + \overline{z}_{\mathrm{a}}\right)^{1/2+\mathrm{i}\mu} = \overline{\mathbf{W}}_{\mathrm{IM}}, \tag{A5}$$

where the $\overline{a}_1$ and $\overline{a}_2$ are given by Lott et al. (2020b, eq. 13) when $\overline{d} = \infty$ and by Soufflet et al. (2022, eq. A12) when $\overline{d} \neq \infty$. Still in Equation (A5), we have

$$\mu = \sqrt{\left|J - \frac{1}{4}\right|} \quad \text{and} \quad \overline{m} = \sqrt{|\overline{k}^2 - J/\overline{d}^2|} \tag{A6}$$

when $J > 1/4$ and when $\overline{k}^2\overline{d}^2 > J$ respectively. When $J < 1/4$, μ is changed to $\mathrm{i}\mu$; and when $\overline{k}^2\overline{d}^2 < J$, $\overline{m}$ is changed to $-\mathrm{i}\,\mathrm{sign}(\overline{k})\overline{m}$. The solution in Equation (A5) corresponds to a "unit amplitude" exponentially decaying mode when $\overline{Z} \to \infty$ (or backward-propagating wave when $\overline{m}$ is imaginary). Near the surface Equation (A5) behaves like the linear combinations of the near critical level solutions of Booker and Bretherton (1967), the critical level being located below the surface (at $Z = -\overline{z}_{\mathrm{a}}$). The function $\overline{\mathbf{W}}_{\mathrm{IM}}$ in Equation (A5) is a matching function that will play a central role in the build up of uniform approximations.

Finally, note that when the shear varies in the far field the hydrostatic approximation is simply obtained by changing $\overline{m}$ in Equation (A6) by

$$\overline{m} = -\mathrm{i}\ \mathrm{sign}(\overline{k})\sqrt{J/\overline{d}}. \tag{A7}$$

A.1.2 Matching region

An important aspect of our work is that there exists a matching region when $\overline{Z}$ is small but above the surface layer where dissipative effects start being significant. In this region, the background wind shear and stratification are almost constant—in dimensional form, see Equation (13)—and we can find an approximate form of the viscous solutions that will match the outer solution and that will allow one to initialize analytically the inner layer numerical integration. In this matching region, the homogeneous parts of Equations 28a–28d are approximated by

$$\mathrm{i}\overline{k}(\overline{Z}+\overline{z}_\mathrm{a})\overline{\mathbf{u}} + \overline{\mathbf{W}} + \mathrm{i}\overline{k}\,\overline{\mathbf{p}} - 2\overline{\lambda}^2\partial_{\overline{Z}}\partial_{\overline{Z}}\overline{\mathbf{u}} = 0. \tag{A8a}$$

$$\mathrm{i}\overline{k}(\overline{Z}+\overline{z}_\mathrm{a})\overline{\mathbf{b}} + J\overline{\mathbf{W}} - \lambda^2\partial_{\overline{Z}}\left(\partial_{\overline{Z}}\overline{\mathbf{b}} + J\partial_{\overline{Z}}\overline{\mathbf{u}}\right) = 0, \tag{A8b}$$

$$\partial_{\overline{Z}}\overline{\mathbf{p}} - \overline{\mathbf{b}} = 0 \quad \text{and} \quad \mathrm{i}\overline{k}\,\overline{\mathbf{u}} + \partial_{\overline{Z}}\overline{\mathbf{W}} = 0, \tag{A8c}$$

which can be approximated by one sixth-order equation for $\overline{\mathbf{W}}$:

$$\begin{aligned} &2\overline{\delta}^6\overline{\mathbf{W}}^{(6)} - 3\mathrm{i}(\overline{Z}+\overline{z}_\mathrm{a})\overline{\delta}^3\overline{\mathbf{W}}^{(4)} - (2-J)\mathrm{i}\overline{\delta}^3\overline{\mathbf{W}}^{(3)} \\ &\quad - (\overline{Z}+\overline{z}_\mathrm{a})^2\overline{\mathbf{W}}^{(2)} - J\overline{\mathbf{W}} = 0. \end{aligned} \tag{A9}$$

To find asymptotic solutions, we follow Koppel (1964) and try the WKB ansatz,

$$\overline{\mathbf{W}}(\overline{Z}) = A(\overline{Z}+\overline{z}_\mathrm{a})\ \mathrm{e}^{B(\overline{Z}+\overline{z}_\mathrm{a})/\epsilon}, \tag{A10}$$

where A and B are functions and ϵ a small parameter. If we use that

$$\begin{aligned} \overline{\mathbf{W}}^{(n)} \approx \Bigg[&\frac{A\dot{B}^n}{\epsilon^n} + n\frac{\dot{A}\dot{B}^{n-1}}{\epsilon^{n-1}} + \frac{n(n-1)}{2}\frac{A\ddot{B}\dot{B}^{n-2}}{\epsilon^{n-1}} \\ &+ O(\epsilon^{2-n})\Bigg]\ \mathrm{e}^{B/\epsilon}, \end{aligned} \tag{A11}$$

a choice that leaves non-degenerated Equation (A9) at the leading order is $\epsilon = \overline{\delta}^{3/2}$. In this case and at order ϵ^{-2} one has

$$2\dot{B}^6 - 3\mathrm{i}(\overline{Z}+\overline{z}_\mathrm{a})\dot{B}^4 - (\overline{Z}+\overline{z}_\mathrm{a})^2\dot{B}^2 = 0. \tag{A12}$$

This admits three solutions corresponding to disturbances that do not grow exponentially in the far field:

$$\dot{B} = 0, \quad \dot{B} = -\sqrt{\mathrm{i}}\sqrt{\overline{Z}+\overline{z}_\mathrm{a}}, \quad \text{and}$$
$$\dot{B} = -\sqrt{\mathrm{i}/2}\sqrt{\overline{Z}+\overline{z}_\mathrm{a}}.$$

When $\dot{B} = 0$, all terms with powers in $\overline{\delta}$ in Equation (A9) are small and give the two inviscid solutions of Booker and Bretherton (1967):

$$(\overline{Z}+\overline{z}_\mathrm{a})^{(1/2)-\mathrm{i}\mu}; \quad (\overline{Z}+\overline{z}_\mathrm{a})^{(1/2)+\mathrm{i}\mu}. \tag{A13}$$

For $\dot{B} \neq 0$, one needs to go to order ϵ^{-1} and obtain

$$\begin{aligned} &\dot{A}[12\dot{B}^5 - 12\mathrm{i}(\overline{Z}+\overline{z}_\mathrm{a})\dot{B}^3 - 2(\overline{Z}+\overline{z}_\mathrm{a})^2\dot{B}] + A[30\ddot{B}\dot{B}^4 \\ &- 18\mathrm{i}(\overline{Z}+\overline{z}_\mathrm{a})\ddot{B}\dot{B}^2 - (2-J)\mathrm{i}\dot{B}^3 - (\overline{Z}+\overline{z}_\mathrm{a})^2\ddot{B}] = 0. \end{aligned} \tag{A14}$$

After substitution of $\dot{B}$ this gives

$$\frac{\dot{A}}{A} = -\frac{9+2J}{4(\overline{Z}+\overline{z}_\mathrm{a})} \quad \text{and} \quad \frac{\dot{A}}{A} = -\frac{5-2J}{4(\overline{Z}+\overline{z}_\mathrm{a})} \tag{A15}$$

for $\dot{B} = -\sqrt{\mathrm{i}}\sqrt{\overline{Z}+\overline{z}_\mathrm{a}}$ and $\dot{B} = -\sqrt{\mathrm{i}/2}\sqrt{\overline{Z}+\overline{z}_\mathrm{a}}$ respectively. This gives two other WKB solutions:

$$\begin{aligned} &(\overline{Z}+\overline{z}_\mathrm{a})^{-(9+2J)/4}\ \mathrm{e}^{-(2/3)\sqrt{\mathrm{i}}[(\overline{Z}+\overline{z}_\mathrm{a})\overline{\delta}]^{3/2}}; \\ &(\overline{Z}+\overline{z}_\mathrm{a})^{-(5-2J)/4}\ \mathrm{e}^{-(2/3)\sqrt{\mathrm{i}/2}[(\overline{Z}+\overline{z}_\mathrm{a})/\overline{\delta}]^{3/2}}. \end{aligned} \tag{A16}$$

The inner solutions having these asymptotic behaviours do not need to be matched to the outer solution because they decay exponentially fast in the vertical; they are mandatory to satisfy the three no-slip surface conditions.

A.1.3 Inner solutions

To evaluate the solution when $\overline{Z} \to 0$, we next introduce the inner layer scale and the inner variables:

$$\begin{aligned} &\overline{\delta} = \left(\frac{\overline{\lambda}^2}{\overline{k}}\right)^{1/3}, \quad \overline{Z}+\overline{z}_\mathrm{a} = \overline{\delta}(\tilde{Z}+\tilde{z}_\mathrm{a}), \quad \overline{\mathbf{W}} = \overline{\delta}\,\overline{k}\,\tilde{\mathrm{W}}, \\ &\overline{\mathbf{p}} = \overline{\delta}\,\tilde{\mathbf{p}}, \quad \overline{\mathbf{u}} = \tilde{\mathbf{u}}, \quad \overline{\mathbf{b}} = \tilde{\mathbf{b}}. \end{aligned} \tag{A17}$$

With these new variables and at leading order, the homogeneous part of Equations 28a–28d transforms into

$$\mathrm{i}\tilde{U}\tilde{\mathbf{u}} + \tilde{U}_{\tilde{Z}}\tilde{\mathrm{W}} = -\mathrm{i}\tilde{\mathbf{p}} + \partial_{\tilde{Z}}2\tilde{\Lambda}\partial_{\tilde{Z}}\tilde{\mathbf{u}}, \tag{A18a}$$

$$\mathrm{i}\tilde{U}\tilde{\mathbf{b}} + J\tilde{U}_{\tilde{Z}}\tilde{\mathrm{W}} = \partial_{\tilde{Z}}\tilde{\Lambda}(\partial_{\tilde{Z}}\tilde{\mathbf{b}} + J\partial_{\tilde{Z}}\tilde{\mathbf{u}}), \tag{A18b}$$

$$\partial_{\tilde{Z}}\tilde{\mathbf{p}} = \tilde{\mathbf{b}}, \quad \text{and} \quad \mathrm{i}\tilde{\mathbf{u}} + \partial_{\tilde{Z}}\tilde{\mathrm{W}} = 0. \tag{A18c}$$

Here, we have also written

$$\begin{aligned} &U \approx \overline{\delta}\tilde{U}, \text{ where } \tilde{U} = \frac{\tilde{\lambda}}{\kappa}\log\left[\frac{\sinh\kappa(\tilde{Z}+\tilde{z}_0)/\tilde{\lambda}}{\sinh\kappa\tilde{z}_0/\tilde{\lambda}}\right], \\ &\tilde{\Lambda} = \tanh\left(\kappa\frac{\tilde{Z}+\tilde{z}_0}{\tilde{\lambda}}\right), \end{aligned} \tag{A19}$$

which take into account that in the inner layer $\overline{U}$ scales as $\bar{\delta}$ and $\overline{U} \approx \overline{U}_{\mathrm{V}}$. As in Lott et al. (2020a), three solutions of Equations A18a–A18c are evaluated numerically using a standard Runge–Kutta algorithm with adaptative vertical mesh, the integrations typically starting around $\tilde{z} \approx 5$ initialized by the matching functions and integrated toward the surface.

More specifically, and to ensure the matching with the outer solution, we first evaluate the inner solution $\tilde{\mathrm{W}}_2$, which almost coincides with the matching function $\overline{\mathbf{W}}_{\mathrm{IM}}$ when $\tilde{Z} \rightarrow \infty$; that is, we initialize the integration with

$$\tilde{\mathrm{W}}_2 \underbrace{\approx}_{\tilde{z}\rightarrow\infty} \tilde{a}_1(\tilde{z}+\tilde{z}_{\mathrm{a}})^{1/2-\mathrm{i}\mu} + \tilde{a}_2(\tilde{z}+\tilde{z}_{\mathrm{a}})^{1/2+\mathrm{i}\mu},$$

$$\text{where} \quad \tilde{a}_1 = \frac{\bar{a}_1}{k}\bar{\delta}^{-1/2-\mathrm{i}\mu}, \quad \tilde{a}_2 = \frac{\bar{a}_2}{k}\bar{\delta}^{-1/2+\mathrm{i}\mu}. \tag{A20}$$

Second, and to permit the satisfying of the three boundary conditions, we also evaluate numerically the two solutions that are exponentially small in the far field; that is, the two solutions $\tilde{\mathrm{W}}_3$ and $\tilde{\mathrm{W}}_4$ with asymptotic behaviours, Equation (A16):

$$\tilde{\mathrm{W}}_3 \underbrace{\approx}_{\tilde{Z}\rightarrow\infty} (\tilde{Z}+\tilde{z}_{\mathrm{a}})^{-(9+2J)/4}\ \mathrm{e}^{-(2/3)\sqrt{\mathrm{i}}(\tilde{z}+\tilde{z}_{\mathrm{a}})^{3/2}}$$

and

$$\tilde{\mathrm{W}}_4 \underbrace{\approx}_{\tilde{Z}\rightarrow\infty} (\tilde{Z}+\tilde{z}_{\mathrm{a}})^{-(5-2J)/4}\ \mathrm{e}^{-(2/3)\sqrt{\mathrm{i}/2}(\tilde{Z}+\tilde{z}_{\mathrm{a}})^{3/2}}. \tag{A21}$$

A.1.4 Uniform approximations

Now that we have inner, matching, and outer solutions, we can build uniform approximations out of the three, but all have to be written with the same coordinate. If we take the outer coordinate for instance, the uniform approximation for the vertical velocity of the outgoing solution can be written

$$\overline{\mathbf{W}}_{2\mathrm{U}}(\overline{Z}) = \overline{\mathbf{W}}_{\mathrm{I}}(\overline{Z}) + \bar{k}\,\bar{\delta}\tilde{\mathrm{W}}_2(\overline{Z}/\bar{\delta}) - \overline{\mathbf{W}}_{\mathrm{IM}}(\overline{Z}), \tag{A22}$$

whereas the uniform approximations of the viscous solution corresponding to $\tilde{\mathrm{W}}_3$ and $\tilde{\mathrm{W}}_4$ simply consist of writing them using outer coordinates, both functions becoming exponentially small in the outer layer (in this case, outer and matching just coincide):

$$\begin{aligned}\overline{\mathbf{W}}_{3\mathrm{U}}(\overline{Z}) &= \bar{k}\,\bar{\delta}\tilde{\mathrm{W}}_3(\overline{Z}/\bar{\delta}),\\ \overline{\mathbf{W}}_{4\mathrm{U}}(\overline{Z}) &= \bar{k}\,\bar{\delta}\tilde{\mathrm{W}}_4(\overline{Z}/\bar{\delta}).\end{aligned} \tag{A23}$$

A.2 Particular solution

A.2.1 Outer solution ($\bar{z} \gg \bar{\delta}$)

When neglecting the viscous terms in Equations 28a–28d, a particular solution is the linear approximation of the difference between the backgrounds expressed in Cartesian and curved coordinates (for the wind the difference $\overline{U}(\bar{z}) - \overline{U}(\overline{Z})$), yielding

$$\begin{aligned}&\bar{\mathbf{u}}_{\mathrm{Ip}} = \bar{\mathbf{z}}\overline{U}_{\overline{Z}}, \quad \bar{\mathbf{b}}_{\mathrm{Ip}} = \bar{\mathbf{z}}\overline{B}_{\overline{Z}}, \quad \bar{\mathbf{p}}_{\mathrm{Ip}} = \bar{\mathbf{z}}\,\overline{B}(\overline{Z}),\\ &\text{and} \quad \overline{\mathbf{W}}_{\mathrm{Ip}} = -\mathrm{i}\bar{k}\,\overline{U}\,\bar{\mathbf{z}}.\end{aligned} \tag{A24}$$

A.2.2 Matching region

In the matching region, this solution is

$$\begin{aligned}&\bar{\mathbf{u}}_{\mathrm{Mp}} = \bar{\mathbf{z}}, \quad \bar{\mathbf{b}}_{\mathrm{Mp}} = J\bar{\mathbf{z}}, \quad \bar{\mathbf{p}}_{\mathrm{Mp}} = J(\overline{Z}+\bar{z}_{\mathrm{a}})\bar{\mathbf{z}},\\ &\text{and} \quad \overline{\mathbf{W}}_{\mathrm{Mp}} = -\mathrm{i}\bar{k}(\overline{Z}+\bar{z}_{\mathrm{a}})\bar{\mathbf{z}}.\end{aligned} \tag{A25}$$

A.2.3 Inner region

In the inner region, we use the scalings in Equations A17 and A19, yielding at leading order

$$\mathrm{i}\tilde{U}\tilde{\mathbf{u}} + \tilde{U}_{\tilde{Z}}\tilde{\mathrm{W}} + \mathrm{i}\tilde{\mathbf{p}} - \partial_{\tilde{Z}}2\tilde{\Lambda}\partial_{\tilde{Z}}\tilde{\mathbf{u}} = \mathrm{i}\tilde{B}\bar{h}, \tag{A26a}$$

$$\partial_{\tilde{Z}}\tilde{\mathbf{p}} - \tilde{\mathbf{b}} = 0, \tag{A26b}$$

$$\mathrm{i}\tilde{U}\tilde{\mathbf{b}} + \tilde{B}_{\tilde{Z}}\tilde{\mathrm{W}} - \partial_{\tilde{Z}}\tilde{\Lambda}(\partial_{\tilde{Z}}\tilde{\mathbf{b}} + J\partial_{\tilde{Z}}\tilde{\mathbf{u}}) = 0, \tag{A26c}$$

$$\mathrm{i}\tilde{\mathbf{u}} + \partial_{\tilde{Z}}\tilde{\mathrm{W}} = 0. \tag{A26d}$$

The particular solution is obtained through numerical integration of Equations A26a–A26d initialized by the particular solution matching the function in Equation (A25). If we call $\tilde{\mathrm{W}}_{\mathrm{Vp}}(\bar{k}, \tilde{Z})$ the solution, a uniform expression of the particular solution can be written

$$\begin{aligned}\overline{\mathbf{W}}_{\mathrm{Up}}(\bar{k}, \overline{Z}) = {}&\overline{\mathbf{W}}_{\mathrm{Ip}}(\bar{k}, \overline{Z}) + \bar{k}\,\bar{\delta}\tilde{\mathrm{W}}_{\mathrm{Vp}}(\bar{k}, \overline{Z}/\bar{\delta})\\ &- \overline{\mathbf{W}}_{\mathrm{Mp}}(\bar{k}, \overline{Z}),\end{aligned} \tag{A27}$$

with similar expressions for $\bar{\mathbf{u}}_{\mathrm{Up}}$ and $\bar{\mathbf{b}}_{\mathrm{Up}}$.

A.3 Boundary conditions

We then rewrite the complete flow fields combining linearly the three homogeneous uniform solutions and the particular uniform solution,

$$\begin{aligned}\overline{\mathrm{W}}(\overline{X}, \overline{Z}) = \int_{-\infty}^{+\infty} \Big[&f_2(\bar{k})\overline{\mathbf{W}}_{2\mathrm{U}}(\bar{k}, \overline{Z})\\ &+ f_3(\bar{k})\overline{\mathbf{W}}_{3\mathrm{U}}(\bar{k}, \overline{Z})\\ &+ f_4(\bar{k})\overline{\mathbf{W}}_{3\mathrm{U}}(\bar{k}, \overline{Z})\\ &+ \overline{\mathbf{W}}_{\mathrm{pU}}(\bar{k}, \overline{Z})\Big]\ \mathrm{e}^{\mathrm{i}\bar{k}\,\overline{X}}\ d\bar{k},\end{aligned} \tag{A28}$$

with similar expressions for $\overline{\mathbf{u}}$, $\overline{\mathbf{b}}$, and $\overline{\mathbf{p}}$. With this notation, the surface conditions in Equation (29) give

$$\begin{aligned}f_2(\overline{k})\overline{\mathbf{W}}_{2\mathrm{U}}(\overline{k},0)+f_3(\overline{k})\overline{\mathbf{W}}_{3\mathrm{U}}(\overline{k},0)\\ +f_4(\overline{k})\overline{\mathbf{W}}_{4\mathrm{U}}(\overline{k},0)=-\overline{\mathbf{W}}_{\mathrm{Up}}(0),\end{aligned} \tag{A29}$$

with similar expression for $\overline{\mathbf{u}}$ and $\overline{\mathbf{b}}$. The three relations obtained for each $\overline{k}$ permit one to evaluate the coefficients $f_i(\overline{k})$ and reconstruct the wave field after inverse Fourier transform and interpolation on the rectangular grid.